

Robust Segmentation of Overlapping Cells in Histopathology Specimens Using Parallel Seed Detection and Repulsive Level Set

Xin Qi*, *Member, IEEE*, Fuyong Xing, David J. Foran, *Member, IEEE*, and Lin Yang, *Member, IEEE*

Abstract—Automated image analysis of histopathology specimens could potentially provide support for early detection and improved characterization of breast cancer. Automated segmentation of the cells comprising imaged tissue microarrays (TMAs) is a prerequisite for any subsequent quantitative analysis. Unfortunately, crowding and overlapping of cells present significant challenges for most traditional segmentation algorithms. In this paper, we propose a novel algorithm that can reliably separate touching cells in hematoxylin-stained breast TMA specimens that have been acquired using a standard RGB camera. The algorithm is composed of two steps. It begins with a fast, reliable object center localization approach that utilizes single-path voting followed by mean-shift clustering. Next, the contour of each cell is obtained using a level set algorithm based on an interactive model. We compared the experimental results with those reported in the most current literature. Finally, performance was evaluated by comparing the pixel-wise accuracy provided by human experts with that produced by the new automated segmentation algorithm. The method was systematically tested on 234 image patches exhibiting dense overlap and containing more than 2200 cells. It was also tested on whole slide images including blood smears and TMAs containing thousands of cells. Since the voting step of the seed detection algorithm is well suited for parallelization, a parallel version of the algorithm was implemented using graphic processing units (GPU) that resulted in significant speedup over the C/C++ implementation.

Index Terms—Level set, mean shift, parallel computing, seed detection, segmentation.

I. INTRODUCTION

BREAST cancer is one of the most frequently diagnosed cancers in women. Approximately 209 060 new cases of invasive breast cancer were reported in women in the U.S. during 2010. There is more than a 98% 5-year relative survival rate when localized breast cancer is detected before it spreads to other parts of the body [1]. Tissue microarrays (TMAs) are a relatively new technology for arranging small histological sections (histospots) in a matrix configuration on a recipient paraffin block [2], [3]. TMAs provide an efficient method for preserving tissue while facilitating high throughput of multiple tissue samples in parallel [4]–[8]. Digital microscopy is a complementary technology that is now generally accepted as a reliable tool for visualizing [8], archiving, and sharing [9]–[11] pathology specimens including TMAs.

Segmenting individual cells in digitized histopathology specimens is usually the first step that is required in automatic image analysis. Recently, an unsupervised clustering approach that utilizes both color and texture features to segment prostate cancer specimens was proposed in [12]. A computationally efficient approach that exploits color and differential invariants to assign class posterior probabilities to delineate the epithelial nuclei, stroma, and background regions in breast microarray was reported in [13]. Segmentation of color and multispectral images was later proposed by combining spatial clustering and vector level set active contours to assess prostate cancer samples in [14].

Each of these segmentation methods produced good results on regions exhibiting little or no cell crowding; however, they often failed to separate touching cells accurately. The watershed family of algorithms has become one of the most commonly used segmentation methods to address the challenge of touching cells. However, the primary limitation of the watershed approaches is that they often result in over segmentation. Some algorithms such as marker-controlled watershed correction [15], [16], rule-based strategies [17]–[19] were developed to address this problem by merging oversegmented regions, but it is difficult to derive a generalized rule to merge oversegmented patches across image ensembles. Evolving generalized Voronoi diagrams [15], [20], [21] that utilize image intensity and geometric information was recently investigated to segment 2-D and 3-D images containing overlapping cells. Li *et al.* [22] presented a gradient flow tracking algorithm for segmenting cell

Manuscript received August 18, 2011; revised October 21, 2011; accepted November 28, 2011. Date of publication December 9, 2011; date of current version February 17, 2012. This research was funded, in part, by grants from the National Institutes of Health through contract 9R01CA156386-05A1 from the National Cancer Institute; and contracts 5R01LM009239-04 and 3R01LM009239-03S2 from the National Library of Medicine. Additional support was provided by a gift from the IBM International Foundation and by the Foundation of the University of Medicine and Dentistry of New Jersey (UMDNJ) under Grant #66-09. Asterisk indicates corresponding author.

*X. Qi is with the Department of Pathology and Laboratory Medicine, the Center for Biomedical Imaging and Informatics, and The Cancer Institute of New Jersey, University of Medicine and Dentistry New Jersey (UMDNJ)-Robert Wood Johnson Medical School, Piscataway, NJ 08854 USA (e-mail: xinqi2000@gmail.com).

F. Xing is with the Department of Electrical and Computer Engineering, Rutgers University, Piscataway, NJ 08854 USA (e-mail: edmundxing@gmail.com).

D. J. Foran is with the Department of Pathology and Laboratory Medicine, the Center for Biomedical Imaging and Informatics, and The Cancer Institute of New Jersey, University of Medicine and Dentistry New Jersey (UMDNJ)-Robert Wood Johnson Medical School, Piscataway, NJ 08854 USA (e-mail: djf.foran@gmail.com).

L. Yang is with the Department of Radiology and the Center for Biomedical Imaging and Informatics, University of Medicine and Dentistry New Jersey (UMDNJ)-Robert Wood Johnson Medical School, Piscataway, NJ 08854 USA (e-mail: linyang711@gmail.com).

Digital Object Identifier 10.1109/TBME.2011.2179298

nuclei in 3-D microscopic images. Although those methods were designed to segment images where the nuclei were closely juxtaposed or touching slightly, they are not suitable for specimens containing large numbers of cells with extensive overlapping areas. A double threshold-based watershed and statistical analysis for clustered cell segmentation was proposed in [17]. This algorithm measures the quality of the resulting segmentation using statistical analysis and provides feedback to correct errors. However, this algorithm relies on the assumption that all cells are similar or belong to a limited number of classes or cell types. Wen *et al.* [23] later reported a study on decomposing clumps of nuclei using high-level geometric constraints derived from maximum curvatures. This approach was very effective in separating touching objects. Unfortunately, its use is somewhat limited because within some touching cells, the common connecting regions do not exhibit local maximal curvatures.

Kothari *et al.* [24] proposed a semiautomatic method for touching cell segmentation, which applied concavity detection at the edge of clusters to find the points of overlap between two nuclei. An ellipse-fitting technique was applied to segment the concavities between two nuclei with overlapping regions. However, the ellipse used in these studies is unable to accommodate the shape of some cells, especially irregularly shaped cancerous cells. Diaz *et al.* [25] reported their study to split overlapping cells using template matching. In this paper, maximal correlation points between the overlapping and template shapes were determined by affine registration. The template size varied from 70% to 120% to find the “best match.” Our team [26] proposed an approach to address touching cell segmentation using concave vertex graphs, and several other graph-based methods were proposed in [27]–[29] to segment touching stem cells in fluorescence microscopy images. Unfortunately, such graph-based methods generally require the image to exhibit a high contrast at the edges of the structure of interest which is often not the case, especially in cancerous regions of the tissue. Elter *et al.* [30] had proposed a method called maximum-intensity linking for segmenting touching cells. This approach is based on the idea of representing an image as a directed graph structure that is significantly faster than classic watershed algorithms; however, it still results in oversegmentation and requires complicated postprocessing steps when used in our experiments. Al-Kofahi *et al.* [31] reported an automatic segmentation of cell nuclei in histopathology images. Their seed detection results were used as initialization markers for nuclear segmentation. Their approach achieved very good results on heterogeneous regions.

Level set-based deformable methods have been widely used for cell segmentation [32]–[34] and different terms [35]–[38] were inserted into original Mumford–Shah function to try to address the overlapping object segmentation problem. Parametric texture adaptive snakes were proposed in [21] for cell segmentation and tracking. However, for the level set-based algorithm or parametric snake to work properly, a good initialization is required to locate each touching object.

A preliminary version of our work was presented in the 2010 High Performance Computing Workshop associated with Medical Image Computing and Computer Aided Intervention [39]. Compared to the shorter conference version which focused on

parallel computing, each step of the proposed algorithm is explained in detail in this paper. Epithelial region extraction and connect component analysis have been newly introduced in the journal version for more efficient parallelization of cellular level segmentation to support whole slide images. Different tissue types prepared with a range of different stains were used to test the effectiveness of the algorithm through exhaustive experiments. The studies were completely redesigned to compare the proposed algorithm with five state-of-arts segmentation methods. An extensive evaluation of seed detection and the selection of a feasible range of parameters were investigated and added in this paper. The algorithm has now been tested on a set of comprehensive, large scale datasets. The contributions are as follows.

- 1) A computationally efficient mean-shift-based single-pass voting algorithm that provides accurate seed detection and robust touching object localization used as an initialization for the repulsive level set model.
- 2) A segmentation framework that can successfully separate cells residing in a densely touching regions. The algorithm has been tested on a large clinical dataset using a range of different tissues and stain preparations.
- 3) The algorithm is designed for easy parallelization as a result of data independence. The graphic processing unit (GPU) parallel version of the seed detection part in the algorithm can process a 1392×1040 image that contains hundreds of touching cells in less than 0.2 s.

II. TOUCHING CELL SEGMENTATION

We propose a novel algorithm for separating touching cells, which is not limited to a specific type of staining preparation. Breast TMAs and blood smears have been acquired using standard RGB imaging with a $40\times$ magnification objective. Standard hematoxylin staining was applied to breast TMA specimens, and the commonly used Giemsa stain was used to prepare peripheral blood smears. Please note that Giemsa stain is a mixture of methylene blue, eosin, and azure B. It is the most dependable stain for differentiating nuclear and/or cytoplasmic morphology of platelets, RBCs, WBCs, etc.

The algorithm was tested on whole slide digitized TMA specimens. In Fig. 1, we show the entire procedure describing the method used to automatically zoom in and crop a single disc from the TMA array using our previous algorithm [40]. Fig. 2 shows some typical overlapping patches in hemotoxylin-stained breast TMA disc. Many patches are shown to contain overlapping regions that are darker than the intensity of nonoverlapping regions. The overlapping regions in this figure are marked with yellow rectangles.

The touching cell segmentation algorithm that we developed is composed of two steps. The first step is to automatically locate the geometric center of each cell using a novel single-pass voting with mean-shift-based seed detection. The result of this step is used as an initial position for the second step that is touching cell segmentation, which extracts each contour of touching cells using a level set function with a repulsion force to penalize any object overlap. The flow chart of whole

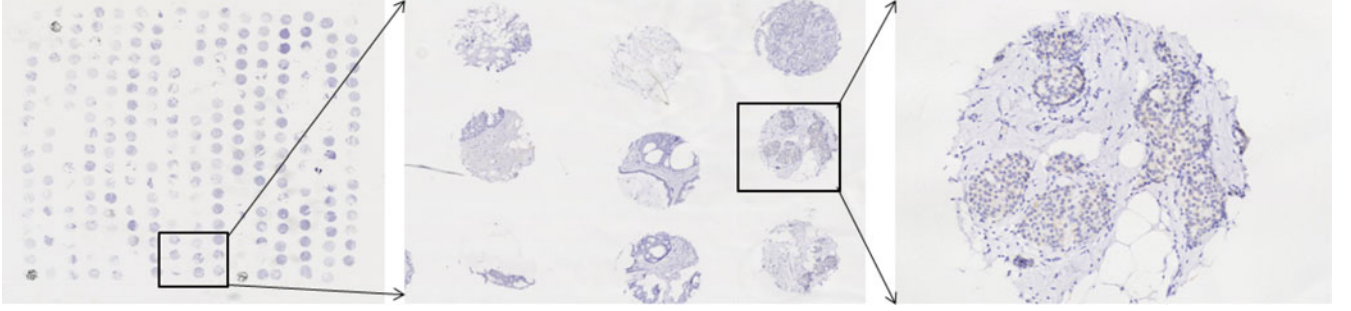


Fig. 1. Procedure on how to automatically zoom in and crop a single disc from the TMA array. The TMA whole slide images were taken under 40 \times objective using Trestle MedMicro system.

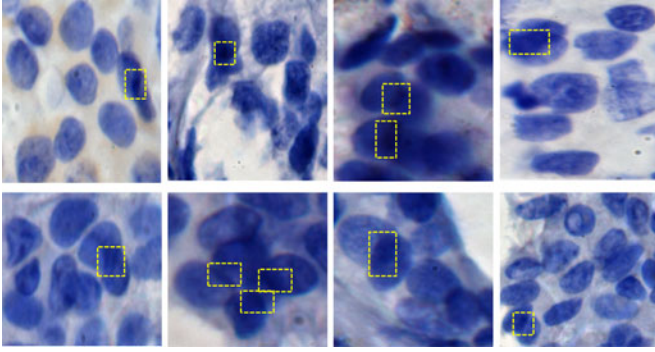


Fig. 2. Representative examples of hematoxylin-stained breast TMA RGB images acquired using a 40 \times objective using a Nikon microscope. Some cells overlap with each other and the intensity of overlapping regions are darker than the intensity of nonoverlapping regions. The overlapping regions are marked with yellow rectangles.

touching cell segmentation is shown in Fig. 3. It contains the epithelium region segmentation [41], seed detection, connect component analysis, and the level set-based contour extraction. The connect component analysis step is intentionally added into the algorithm. By separating the whole disc into connected components, the algorithm can be run in parallel on multiple cores and the final segmentation result is an ensemble of all the connected components. GPU was applied to speed up the entire segmentation procedure.

A. Seed Detection

Since the number and location of cells are not known, *a priori*, it is difficult to directly segment cells from microscopic images especially when they touch one another. The geometric centers of cells are considered as a basic perceptual cue that is used by human experts to support the accurate separation of touching cells. Al-Kofahi *et al.* [31] reported a distance-constrained Laplacian-of-Gaussian (LoG) filtering method to identify the center of nuclei. Parvin *et al.* [42] proposed an iterative voting method that was used to detect the centers of touching cells.

The method in [31] produced excellent results in detecting the nuclear seed points using a distance-map constrained multiscale LoG filtering. The algorithm could lead to undersegmentation for some homogenous regions with multiple nuclei. Therefore, the authors provide a postprocessing module that requires human interaction to “fix” some segmentation errors. The method

in [42] provides excellent results in detecting the centers in touching cells exhibiting homogenous intensity; however, when the intensity of overlapping regions is brighter (or darker) than the nonoverlapping regions within individual cells, a set of false seeds will be created in the overlapping regions. This is not surprising because the voting schema in [42] is biased toward the boundary of the object. The edges of overlapping regions contribute to the creation of false seeds within the overlapping regions using methods by Parvin *et al.* [42]. We will explain in detail how we are able to address this problem, and we will also show the significant improvement of the new algorithm that applies a shifted Gaussian kernel and mean shift onto single-pass voting to generate more accurate and quicker seed detection, for both synthetic and real testing datasets.

Defining $I(x, y)$ as the original image, the image gradient $\nabla I(x, y)$ and the magnitude $\|\nabla I(x, y)\|$ are subsequently calculated. Because typically the background of original images can be converted to black or darker than the intensity of objects of interest, the direction from outside of object to center of object is negative for this definition. For each pixel (x, y) , the voting direction $\alpha(x, y)$ is defined as the negative gradient direction $-\nabla I(x, y)/\|\nabla I(x, y)\| = -(\cos(\theta(x, y)), \sin(\theta(x, y)))$ where θ is the angle of the gradient direction with respect to x -axis. The voting area $A(x, y; r_{\min}, r_{\max}, \Delta)$ of each pixel is defined by a cone shape with its vertex at (x, y) . A cone-shaped voting area was chosen for two reasons. First, the center of the cell is far away from its boundary; thus, more voting points are located within the region closest to the center rather than within the region closest to the edge of the cell. Second, a cone-shaped voting area greatly reduces the time requirement by reducing the number of calculations since there are fewer voting points in total. The $r_{\min}, r_{\max}, \Delta$ and voting area of pixel (x, y) are illustrated in Fig. 4. We define a 2-D Gaussian kernel $g(x, y, \mu_x, \mu_y, \sigma)$ with its mean (μ_x, μ_y) located at the center of the voting area and oriented in the voting direction $\alpha(x, y)$. The shifted Gaussian kernel is defined as

$$g(x, y, \mu_x, \mu_y, \sigma) = \frac{1}{2\pi\sigma^2} \exp\left(-\frac{(x - \mu_x)^2 + (y - \mu_y)^2}{2\sigma^2}\right) \quad (1)$$

where $\mu_x = x + (r_{\max} + r_{\min}) \cos \theta/2$ and $\mu_y = y - (r_{\max} + r_{\min}) \sin \theta/2$. We designed the kernel in this manner so that voting is amplified at the center of the targeted object.

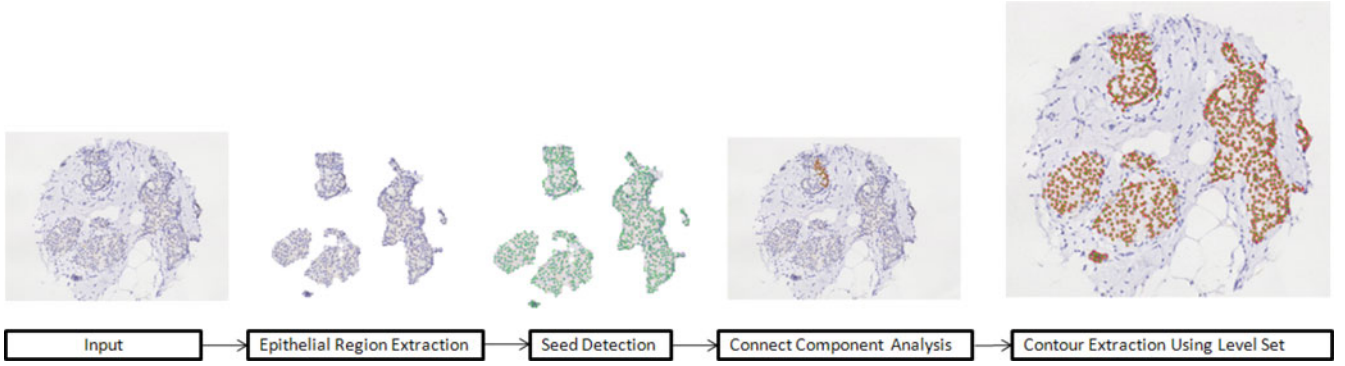


Fig. 3. Flow chart for the automated segmentation of overlapping cells in hemotoxylin-stained breast TMA discs. From left to right, it contains input image; extracted epithelial region of input image; seed detection results with green dots representing the detected seeds; cell contours of the biggest connected component within the epithelial region; and final segmentation results of an ensemble of all the connected components.

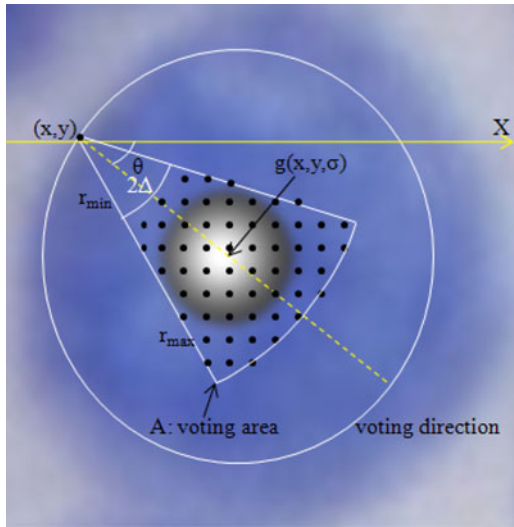


Fig. 4. Cone-shaped voting area with the Gaussian kernel overlapped at the center of the voting area.

We define $V(x, y; r_{\min}, r_{\max}, \Delta)$ as the voting image, which has the same dimensions as the original image $I(x, y)$. Setting an initialization of V as zero for all pixels (x, y) , for each pixel (x, y) , we update the voting image in a single-pass approach as

$$V = V(x, y; r_{\min}, r_{\max}, \Delta) + \sum_{(u,v) \in A} \|\nabla I(x, y)\| g(u, v, \mu_x, \mu_y, \sigma). \quad (2)$$

Using this single-pass voting approach, the geometric centers of objects are determined by executing mean shift on the sum of the voting images. The detailed algorithm is listed in Algorithm 1.

Although our study was initially motivated by [42], the method we propose differs because of several significant aspects: 1) For each point (x, y) with high gradient, we define a shifted Gaussian kernel at the center of the voting area instead of (x, y) . This is a critical step that enables the new algorithm to provide accurate results for overlapping cells in histopathology specimens. As the center of the object is usually far from the boundary, the shifted Gaussian kernel encourages the voting toward the center of the object and thereby avoids false seeds

Algorithm 1: Single-pass voting with mean shift based seed detection

1. Initialize the parameters: d is the estimated average diameter of cells within the image, $r_{\min} = 0.5d$, $r_{\max} = 1.5d$, $\Delta = 30$.
2. Calculate the Gaussian blurred gradient image and the orientation of the gradient at each pixel (x, y) . Record the set of (x, y) with large gradient magnitude as S .
3. For each point $(x, y) \in S$, calculate the voting image $V(x, y)$ in a single-pass way.
4. for $R = 0.3, 0.4, \dots, 0.9$ do
5. Record all the points (x, y) in the voting image with voting number larger than $\max(V(x, y)) \times R$.
6. end for
7. Sum all the voting images and run mean shift to generate the final list of the seeds. The bandwidth of the mean shift is defined as 1/3 of the estimated average diameter of the cells.

in overlapping regions (we revisit this issue in the experimental section for clarity). For the overlapping regions, the overlapped edges always exhibit higher gradient intensity values than other regions. The shifted Gaussian kernel causes high voting outside of overlapping regions instead of inside; thus, the algorithm reduces false seeds. 2) Instead of using iterative voting as reported in [42], we calculate the centers of overlapping objects by running mean shift on the single-pass voting images. This step dramatically reduces the computational time of processing as many iteration steps are avoided. More importantly, using single-pass voting with mean shift to replace iterative voting facilitates subsequent parallelization. In Fig. 5, we show the entire process of the seed detection applying single-pass voting with mean shift to generate the final seed. The false seed on the overlapping region is marked with a yellow square (using diameter = 50, Sigma = 3, and minimal voting = 550 in the most recent release of ImageJ plugin using Parvin's algorithm [42]).

B. Parallelization of the Seed Detection on the Graphic Processing Unit

During the seed detection step, each voting pixel (x, y) utilizes a cone-shaped voting area $A(x, y; r_{\min}, r_{\max}, \Delta)$. Each pixel in the final voting image V is then updated by (2).

After calculating the execution time profile for each step in the proposed seed detection algorithm, we found that the most computationally expensive part is the calculation of the voting image (90% of the whole procedure). Because our voting image is

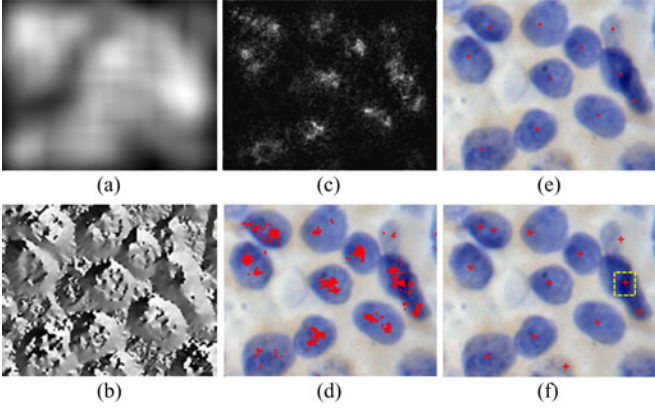


Fig. 5. Whole process of the seed detection applying single-pass voting with mean shift to generate the final seeds. (a) Magnitude of the gradient image. (b) Angular image of the gradient direction with respect to x -axis. (c) Summed voting images, and the white points show the number of candidate seed points. (d) Voting points superposed on its original image before mean shift. (e) Final detected seeds superposed on the original image after mean shift. (f) Detected seeds superposed on the original image using Parvin's algorithm [42].

calculated using single pass with mean shift rather than iterative voting, it is much more computationally efficient. Furthermore, because the voting algorithm is a pixel-based method that has an advantage of easy parallelization as a result of *data independence*, this part can be accelerated by introducing parallelization on a GPU. In our algorithm, we utilized eight blocks for a GPU. Within each block, we create 128 threads. Each voting pixel was assigned to one thread to calculate its corresponding voting image. In total 1024 threads were created simultaneously. In this way, the GPU accelerated the voting image calculation dramatically and, therefore, increased the entire seed detection procedure dramatically.

C. Cell Segmentation

Because of the accuracy of the detected seeds (the geometric centers of cells), the touching cell segmentation process was performed using level set based on an interactive model. The interactive model includes two types of mechanisms: 1) a repulsion term to prevent the contours of adjacent cells from overlapping and separating the touching cell boundaries; 2) the competition term to determine the membership of each pixel that is assigned to the cell producing the smallest difference. Considering an image I that has N cells, let $C_i (i = 1, \dots, N)$ denote the contours that evolve toward the boundaries. Please note that each cell is represented by its own level set energy function. Instead of examining each contour independently, the interactive between neighboring contours was integrated into the level set energy function. The energy function E for cell segmentation combines the repulsion and competition terms and can be expressed as follows:

$$E = \lambda_0 \sum_{i=1}^N \int_{in(C_i)} |I - c_i|^2 dx dy + \lambda_b \sum_{i=1}^N \int_{\Omega_b} |I - c_b|^2 dx dy$$

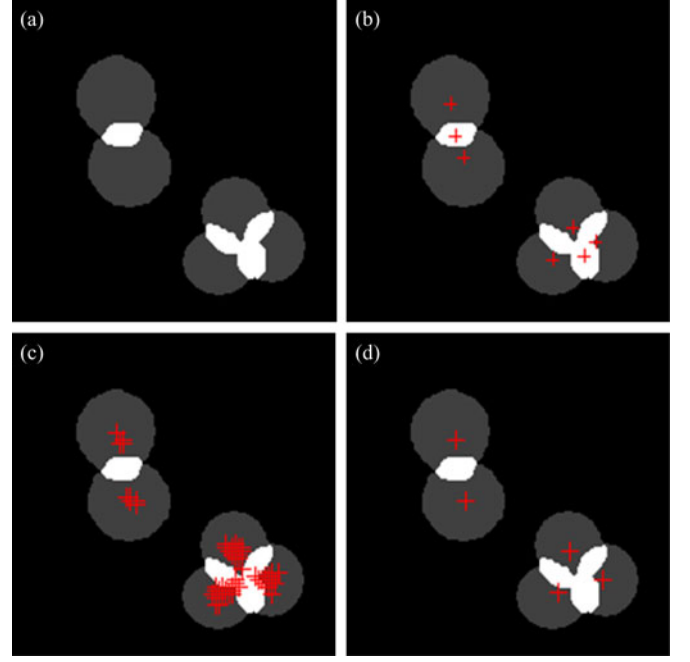


Fig. 6. Seed detection results for a representative synthetic image. The red crosses denote detected seeds. (a) Original synthetic image. (b) Seed detection results using the iterative voting method in [42]. (c) Intermediate results of our method. (d) Final detected seeds using our single pass with the mean-shift-based seed detection method.

$$+ u \sum_{i=1}^N \int_0^1 g(|\nabla I(C_i(q))|) |C'_i(q)| dq + \omega \sum_{i=1}^N \sum_{j=1, j \neq i}^N A_i \cap A_j \quad (3)$$

where A_i denotes region of cell $\{A_i | i = 1, 2, \dots, N\}$ and Ω_b is the background that represents the region outside all the cells $out(C_1) \cap out(C_2) \cap \dots \cap out(C_N)$. The operator $in()$ and $out()$ represent the regions inside and outside of cells, respectively. The c_i and c_b are the mean intensities of the cell region and background region, respectively. The λ_0 , λ_b , and u are the fixed weighting parameters. Function g is chosen to be a sigmoid function

$$g(x) = (1 + e^{\frac{x-\beta}{\alpha}})^{-1} \quad (4)$$

where α is used to control the slope of the output curve and β controls the window size. By penalizing the union of the overlapped region $\{A_i | i = 1, \dots, N\}$ enclosed by contours $C_i (i = 1, \dots, N)$, the last item in Energy function E is the repulsion term that is used to represent the repulsion force between each adjacent touching object and the ω is the regulation parameter.

Segmentation is achieved by minimizing the energy function E using the evolution of the level set. In order to express the energy function using level set, we introduced the regularized Heaviside function H [43]

$$H_\epsilon(z) = \frac{1}{2} \left(1 + \frac{2}{\pi} \arctan \left(\frac{z}{\epsilon} \right) \right) \quad (5)$$

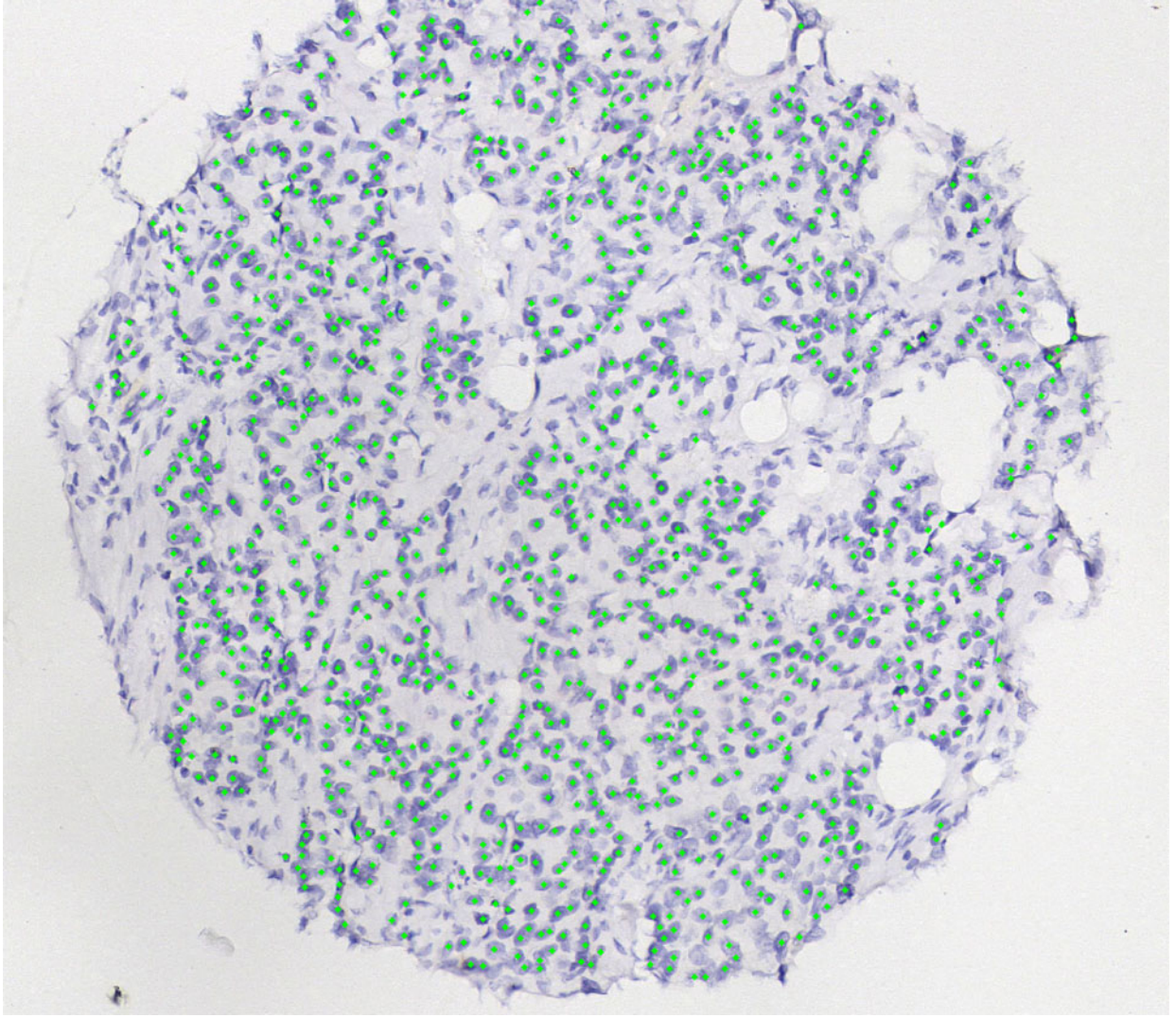


Fig. 7. TMA whole disc seed detection results using our proposed method. The green dots represent the detected seeds on a whole TMA breast core acquired using a 10 \times objective. Please note that these are the seed detection results overlaid on the segmented epithelial region mask as was shown in the first step in Fig. 3. Those seeds falling outside the epithelial region masks were intentionally excluded and are not the result of a missed detection.

where ε is the regulation parameter of the Heaviside function and delta function is defined as

$$\delta_{\varepsilon}(z) = \frac{d}{dz} H_{\varepsilon}(z). \quad (6)$$

The energy function can be minimized by iteratively employing the gradient descent method. The evolution equation for each energy function $\Psi_i(t, x, y)$ is then obtained by deducing the associated Euler-Lagrange equation as

$$\begin{aligned} \frac{\partial \Psi_i}{\partial t} = & \delta(\Psi_i) \{ \lambda_o |I - c_i|^2 - \lambda_b |I - c_b|^2 \prod_{j=1, j \neq i}^N H(\Psi_j) \\ & + \mu \nabla g \cdot \frac{\nabla \Psi_i}{|\nabla \Psi_i|} + \gamma g \operatorname{div} \left(\frac{\nabla \Psi_i}{|\nabla \Psi_i|} \right) \\ & + \omega \sum_{j=1, j \neq i}^M (1 - H(\Psi_j)) \}. \end{aligned} \quad (7)$$

After evolving the level set contours, the means c_i and c_b of the cell and background regions are iteratively updated. This method was proposed and proved to be quite effective and accurate for RNAi fluorescent cellular image segmentation in [38]. Throughout the experiments, the parameters that we selected were: $\lambda_0 = 1$, $\lambda_b = 0.3$, $\mu = 0.5$, $\gamma = 0.2$, $\omega = 0.6$, $\epsilon = 1$, $\alpha = 1$, $\beta = 7$ empirically.

III. EXPERIMENTAL RESULTS

Hematoxylin-stained breast TMA specimen images were captured at a high magnification objective (40 \times) using a Nikon microscope. In total there were 234 image patches containing more than 2200 image cells.

A. Seed Detection

To illustrate the new seed detection method that we developed, an example of a synthetic image with five overlapping objects is shown in Fig. 6. Fig. 6(a) is the original synthetic

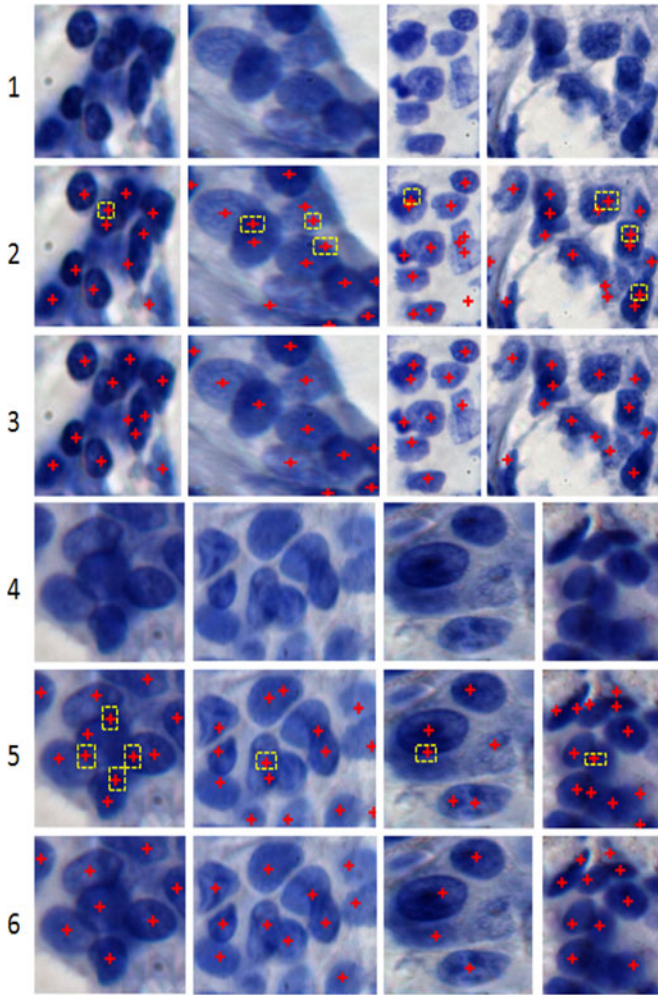


Fig. 8. Seed detection results of hematoxylin-stained pathology specimens. The first and the fourth rows are the region of interest of the original images; the second and fifth rows are the seed detection results using [42]; the third and sixth rows are the seed detection results using our method. The seeds are marked with red color. The false detected seeds are marked with yellow rectangles.

image, with two and three overlapping cells, respectively. Fig. 6(b) is the seed detection results using the iterative voting method in [42], which created false seeds in the two overlapping areas. Fig. 6(c) is the intermediate results of our method before applying mean shift clustering, and Fig. 6(d) is the final detected seeds using our method. From this experiment, it can be seen that the iterative voting method [42] tends to put the seeds at the overlapping regions [shown in Fig. 6(b)] when overlapping regions have brighter/darker intensity than its corresponding touching objects. Using our method as shown in Fig. 6(d), the detected seeds are approximately located in the centers of the objects and no seeds were misdetected in the overlapping regions. In the real dataset (hematoxylin-stained pathology specimens), there are cases where the overlapping areas are darker than the intensity of the nontouching cells as shown in Fig. 2.

In Fig. 7, hundreds of cells were accurately detected on the epithelial region. For better illustration, we cropped several patches from the whole dataset and show their comparative seed detection results in Fig. 8 using [42] and our method. It is obvious

that the method in [42] creates false seeds in the overlapping regions; while the algorithm we developed avoids these errors and provides reliable seed detection results. In Fig. 8, the first and the fourth rows are the original hematoxylin-stained breast TMA images; the second and fifth rows are the seed detection results using [42]. The regions containing false detected seeds are marked in yellow rectangles; the third and sixth rows are the seed detection result using our method. All of the detected seeds are marked with red crosses. In Fig. 9, we show the seed detection results on the whole slide-scanned blood smear slide where thousands of cells are successfully detected. The blood smear image was acquired using 40 \times objective on a Trestle MedMicro system.

In order to gauge the accuracy of seed detection, an error function is defined as the pixelwise distance E between seeds manually located and seeds extracted by seed detection methods. Table I shows the quantitative results of our algorithm and [42] both compared with the ground truth annotation. The 80% column in Table I represents the sorted 80% accuracy among all the seed detection results. Meanwhile a number of missing and false seeds are calculated. When compared with the ground-truth annotation, the mean of the number of missing seeds and false seeds using our algorithm were 0.2 and 0.8, respectively. The mean of the number of missing seeds and false seeds using [42] were 1 and 1.2, respectively.

Due to the minimal diameter r_{\min} of cells and the bandwidth of mean shift played a significant role in our seed detection method, the error function defined earlier was calculated to test the parameter sensitivity of the algorithm. The range of minimal diameter is defined as minus and plus 10 of the estimated minimal diameter of the cell. The range of the bandwidth of mean shift is from 5 to 19. Fig. 10 shows three examples of the average errors respect to the minimal diameter of cells (horizontal axis) and the bandwidth of mean shift (vertical axis). Each row represents one test image and its mean pixelwise detection errors with respect to two parameters: the minimal diameter of cells and the bandwidth of mean shift. From the results in Fig. 10, it is apparent that the errors are relatively insensitive to specific values. Within a feasible range, an average error smaller than 5 pixels is achieved.

B. Segmentation

In Fig. 11, the performance of the proposed touching cell segmentation method is compared with the level set based on an interactive model using the seeds detected by [42]. Each column represents two testing samples. The contours are presented using red lines. Yellow squares are oversegmented regions that arise due to false seeds. The first and the fifth rows are the original hematoxylin-stained pathology specimens; the second and the sixth rows are the ground-truth annotation as provided by human experts; the third and seventh rows are the segmentation results generated by the interactive level set using the seed provided by [42]; the fourth and eighth rows are the segmentation results using single pass with mean-shift-based seed detection and interactive level set.

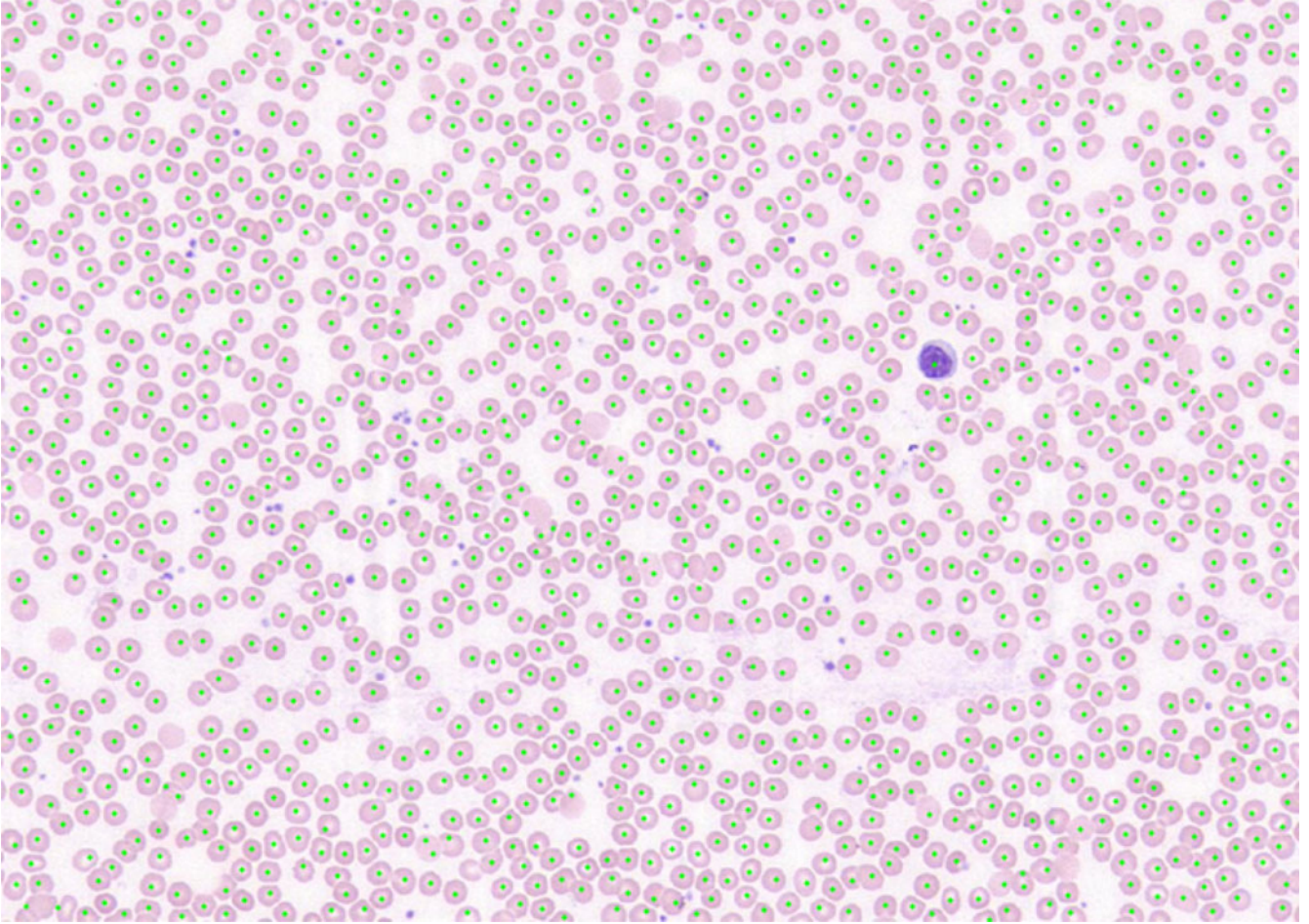


Fig. 9. Whole slide blood smear seed detection results using our proposed method. The stained blood smear image was taken under 40× objective using Trestle MedMicro system.

TABLE I
QUANTIFICATION OF THE PIXELWISE SEED DETECTION ERRORS OF OUR ALGORITHM AND ([42]), BOTH COMPARED WITH THE GROUND TRUTH ANNOTATION OF THE SEEDS

	Mean	Variance	Median	Min	Max	80%
Pixelwise detection error E (Our method)	6.63	4.53	6.81	3.05	10.31	5.08
Pixelwise detection error E ([42])	7.46	7.29	7.75	3.32	12.55	5.23

In order to quantitatively measure the accuracy of this approach, precision P and recall R [44] were calculated for the newly developed touching cell segmentation algorithm and [42], both were compared with the ground-truth annotations. The P is defined as the intersection between the segmentation results and the manually annotation results divided by the segmentation results. The R is defined as the intersection between the segmentation results and manually annotation results divided by the manually annotation results. The mean and standard deviation of P and R for our touching cell segmentation algorithm is 0.90 ± 0.02 and 0.78 ± 0.01 , respectively, which indicates a good agreement between the manual and ground truth annotations. The mean and standard deviation of P and R for interactive level set using the seed provided by [42] is 0.84 ± 0.04 and 0.64 ± 0.02 , respectively.

In Fig. 12, we provide the segmentation results on a whole TMA disc, for illustration purposes we zoom in and crop several

representative patches. In Fig. 13, we show four representative patch image segmentation results of our method as compared to five other algorithms including marker-based watershed, mean shift, isoperimetric [45], and two methods presented in [42] and [31], respectively. Using our seeds, marker-based watershed tends to oversegment the whole cell in the image as it cannot handle the intensity variation within the cells. Mean shift, isoperimetric [45], and method in [31] segmentation tend to undersegment the image by merging multiple cells into one object. Method in [42] tends to create false seeds in the overlapping region of cells, which leads to improperly segment cells in the overlapping regions. All the source codes or binaries of the other state-of-the-art method were implemented by their original authors and downloaded from their websites. In Table II, we show the detailed statistics of the quantitative segmentation results compared with the ground truth annotation. The 80% column in Table II represents the sorted 80% accuracy among

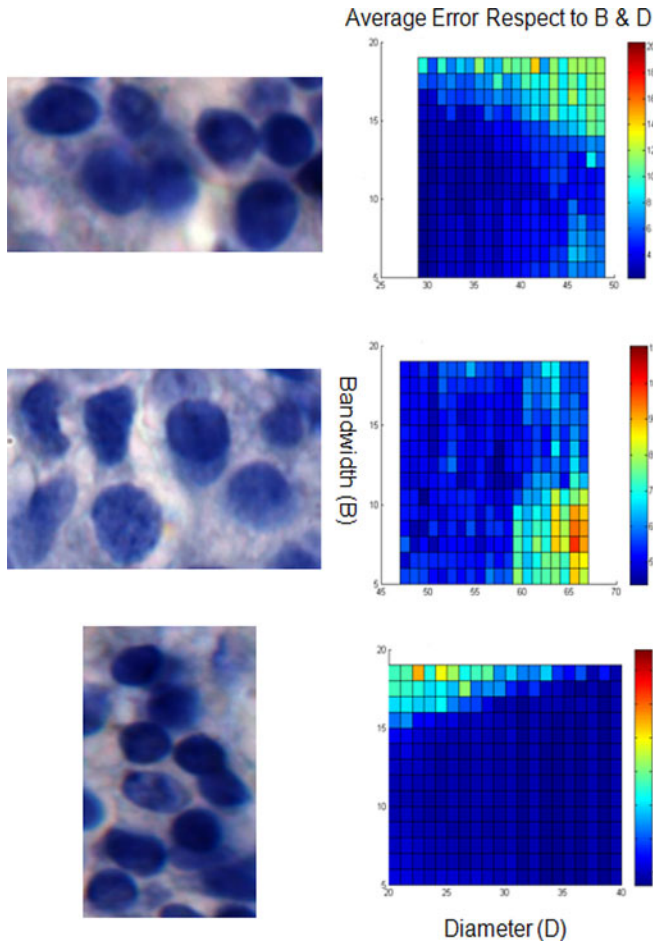


Fig. 10. Three examples of the average error respect to the minimal diameter of cells and the bandwidth of mean shift. The first column is the RGB images; the second column is their corresponding mean errors with respect to the minimal diameter of cells and the bandwidth of mean shift. Within a feasible range, an average error smaller than 5 pixels can be achieved.

all the 234 image patches, which contains around 2200 cells. From Table II, we achieved better segmentation result compared with other methods because of the reduction of false seeds.

The code was parallelized on a GPU. GPU is a massively parallel multicore chip that can execute thousands of concurrent threads. The GPU cores (also called stream processors) are grouped into several streaming multiprocessors. They are managed by the thread manager. The GPU used in these experiments was a NVIDIA Quadro FX5800 that has 240 cores and 30 streaming multiprocessors, each of which contains 8 GPU cores. It supports both single and double float point precision; offers 933 GFlops single precision; and has memory bandwidth with 102 GB/s. Unlike CPU threads that are heavy weight, GPU threads are light weight with little creation overhead, instant switching, and instruction and memory latency hiding. The compute unified device architecture (CUDA) environment from NVIDIA Corporate was utilized throughout the parallel implementations.

The experimental results show significant speedup (22 times faster when compared with the sequential implementation on CPU and thousands of times faster than the original MATLAB

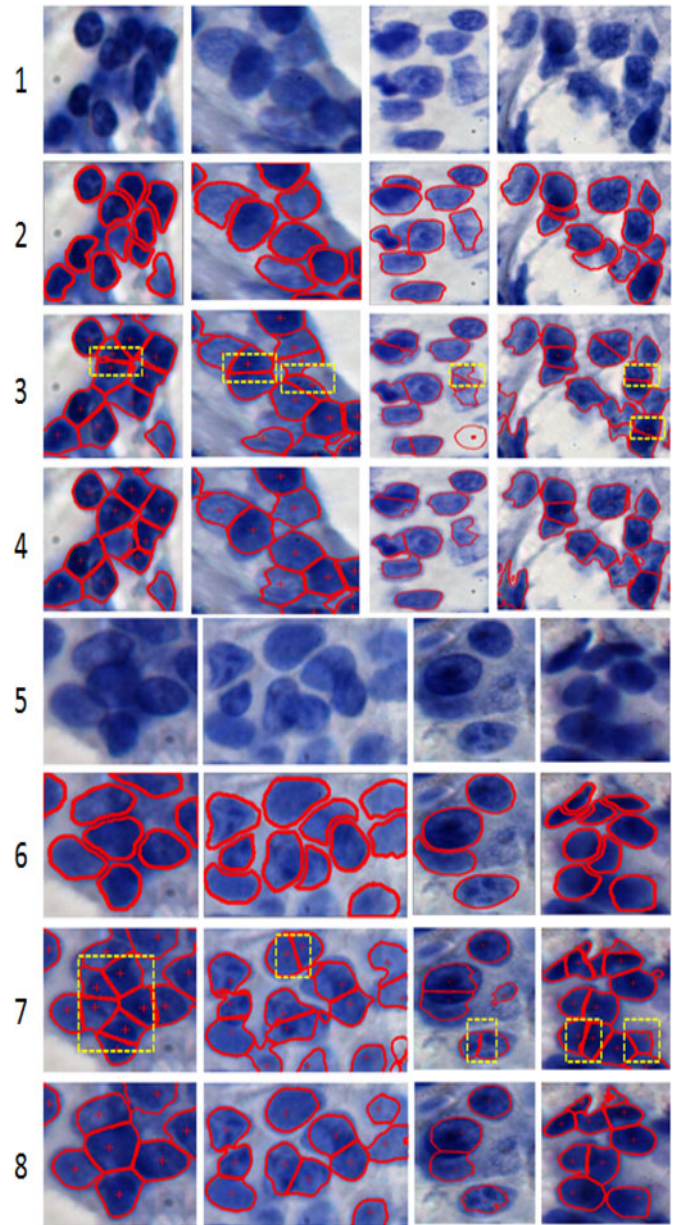


Fig. 11. Segmentation results illustrated using eight images of hematoxylin-stained pathology specimens. Each column represents two testing samples. The contours are presented using red lines. Yellow squares are oversegmented regions due to false seeds. The first and the fifth rows are the original hematoxylin-stained pathology specimens; the second and the sixth rows are the ground truth annotation by human experts; the third and seventh rows are the segmentation results by interactive level set using the seeds provided by [42]; the fourth and eighth rows are the segmentation results using single pass with mean-shift-based seed detection and interactive level set.

implementation). In the parallel version of the algorithm, we can complete the seed detection procedure for an image with dimensionality 1392×1040 in 197 ms. The final repulsive level set algorithm, based on a C/C++ implementation, can process images in less than 5 s.

IV. DISCUSSION AND CONCLUSION

In this paper, we present a touching cell segmentation algorithm using challenging clinical datasets to test performance.

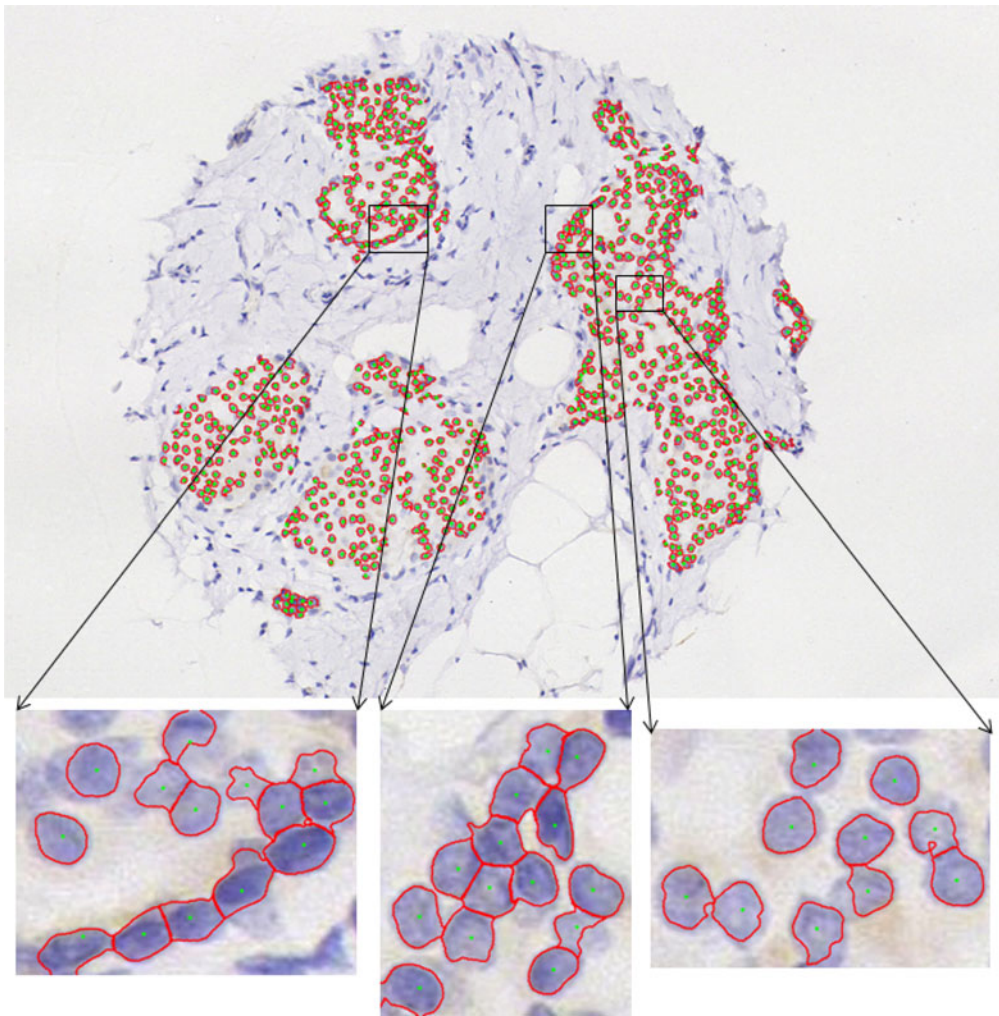


Fig. 12. TMA whole disc segmentation results on epithelial regions. The first row is the hematoxylin-stained whole disc breast TMA. The second row consists of regions that have been enlarged for detailed viewing.

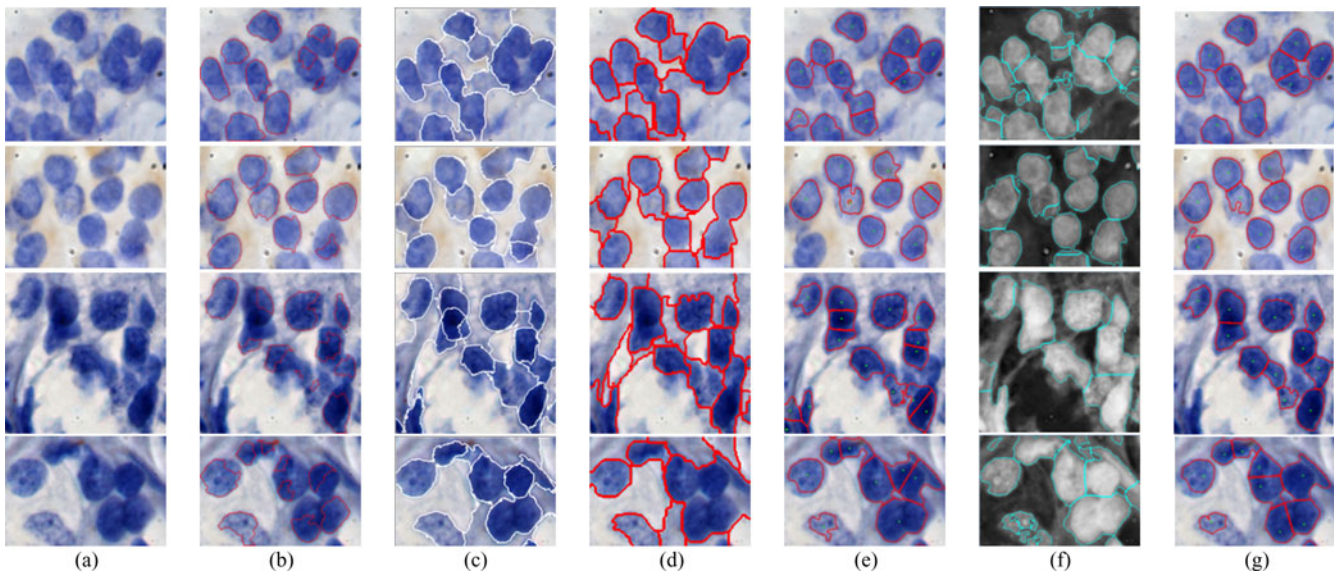


Fig. 13. Comparative segmentation results on four representative images patches. (a) Original image patches. (b) Marker-based watershed segmentation results using our detected seeds. (c) Mean-shift results (d) Isoperimetric segmentation results [45]. (e) Segmentation results using method presented in [42]. (f) Segmentation results using the method described in [31]. (g) Segmentation results using the proposed method.

TABLE II
SEGMENTATION ACCURACY COMPARED WITH GROUND TRUTH ANNOTATION, THE WATERSHED REPRESENTS THE MARKER-BASED WATERSHED ALGORITHM

Precision(P)	Mean	Variance	Median	Min	Max	80%	Recall(R)	Mean	Variance	Median	Min	Max	80%
Our method	0.90	0.02	0.94	0.22	1.00	1.00	Our method	0.78	0.01	0.80	0.20	0.96	0.85
Iterative Voting [42]	0.84	0.04	0.93	0.29	1.00	1.00	[42]	0.64	0.02	0.65	0.28	0.90	0.75
Graph-cut & Coloring [31]	0.82	0.04	0.90	0.18	1.00	0.99	[31]	0.81	0.02	0.87	0.20	0.99	0.93
Isoperimetric [45]	0.87	0.04	0.95	0.23	1.00	1.00	[45]	0.76	0.02	0.80	0.23	0.95	0.87
Mean-shift	0.73	0.07	0.85	0.17	1.00	0.99	Mean-shift	0.78	0.02	0.81	0.26	0.96	0.87
Watershed	0.73	0.03	0.99	0.07	1.00	1.00	Watershed	0.52	0.06	0.54	0.03	0.93	0.78

Accurate seed detection was shown to be a prerequisite for accurate segmentation. We demonstrated that single-pass coupled with mean-shift-based voting algorithm can accurately detect the centers of regions containing densely touching and overlapping cells.

The method in [42] was shown to achieve very good results for homogenous touching objects, even though it was sometimes necessary to tune the parameters. However, when we compared the newly developed seed detection method with the one in [42], where there existed touching cells with nonhomogeneous intensities, the new method produced much better results. The accurate seed detection is the prerequisite to achieve an accurate cellular segmentation. We conducted comparison experiments using our method and Parvin's [42] approach using the software posted on their group's website at <http://www.vision.lbl.gov/>. These studies showed that our seed detection algorithm was not sensitive to parameters initialization as shown in Fig. 10. Within a feasible range, an average errors smaller than 5 pixels can be achieved.

The new segmentation algorithm is not sensitive to the parameters in (7) [38]. Our experiments shown that there is only a slight variation in the performance even if the value of the repulsive weight ω changes more than 50%. Meanwhile, the algorithm performance varies less than 5% when the values of the parameters λ_0 and λ_b vary about 20%. In addition, the parameters μ and γ play minor roles in the performance of the algorithm. However, due to the fact that active contours are local models, they are not robust to the initial positions that are determined by the location of the seeds. That is the central reason why the accurate seed detection is necessary before the level set method is applied to the cell segmentation.

For the cell overlapping regions, the edges have dramatic intensity variation. For the regions within the cells, the intensity variation within the cells is much milder compared to the intensity variation of overlapping regions. The third term in the (7) enhances the edge effects and the fourth term smoothes the contours, which is not sensitive to both noise and mild intensity variation within the cells so that the algorithm can separate touching cells to create smooth and complete contour of each cell. Watershed algorithm can not handle intensity variation within cells very well, which leads to incomplete and jagged contours of touching cells. Consequently, the interactive model outperforms the watershed algorithm even when the watershed is provided with accurate seeds for initialization.

Given these estimated seeds, a level set active contour based on the interactive model can effectively separate each of touching cells. The improved segmentation results are achieved by

accurately estimating the seeds (number of cells) and utilizing a repulsion term in the level set energy function to separate the touching boundaries. The method is automated requiring very little prior knowledge. Therefore, it can be extended to other touching object segmentation applications including a broad range of applications requiring accurate spatial localization of multiple biomarkers that have been tagged with immuno-stains or quantum dot conjugates. The GPU implementation of the seed detection algorithm can handle one 2-D image (1392×1040) in less than 0.2 s. The experimental results show that GPU is an efficient parallel platform for the proposed novel algorithm.

REFERENCES

- [1] A. Jemal, R. Siegel, E. Ward, Y. Hao, J. Xu, and M. J. Thun, "Cancer statistics: 2010," *CA Cancer J. Clin.*, vol. 60, no. 5, pp. 277–300, 2010.
- [2] J. Kononen, L. Bubendorf, A. Kallionimeni, M. Barlund, P. Schraml, S. Leighton, J. Torhorst, M. J. Mihatsch, G. Sauter, and O. P. Kallionimeni, "Tissue microarrays for high-throughput molecular profiling of tumor specimens," *Nature Med.*, vol. 4, pp. 844–847, 1998.
- [3] D. L. Rimm, R. L. Camp, L. A. Charette, J. Costa, D. A. Olsen, and M. Reiss, "Tissue microarray: A new technology for amplification of tissue resources," *Cancer J.*, vol. 7, pp. 24–31, 2001.
- [4] R. L. Camp, L. A. Charette, and D. L. Rimm, "Validation of tissue microarray technology in breast carcinoma," *Lab. Invest.*, vol. 80, pp. 1943–1949, 2000.
- [5] O. P. Kallionemi, U. Wagner, J. Kononen, and G. Sauter, "Tissue microarray technology for high-throughput molecular profiling of cancer," *Human Mol. Genet.*, vol. 10, pp. 657–662, 2001.
- [6] R. L. Parker, D. G. Huntsman, D. W. Lesack, J. B. Cupples, D. R. Grant, M. Akbari, and C. B. Gilks, "Assessment of interlaboratory variation in the immunohistochemical determination of estrogen receptor status using a breast cancer tissue microarray," *Amer. J. Clin. Pathol.*, vol. 117, pp. 723–728, 2002.
- [7] D. M. A. El-Rehim, G. Ball, S. E. Pinder, E. Rakha, C. Paish, J. F. R. Robertson, D. Macmillan, R. W. Blamey, and I. O. Ellis, "High-throughput protein expression analysis using tissue microarray technology of a large well-characterised series identifies biologically distinct classes of breast cancer confirming recent cDNA expression analyses," *Int. J. Cancer*, vol. 116, pp. 340–350, 2005.
- [8] M. V. Iorio, M. Ferracin, C. Liu, A. Veronese, R. Spizzo, E. M. S. Sabbioni, M. Pedriali, M. Fabbri, M. Campiglio, S. Menard, J. P. Palazzo, A. Rosenberg, P. Musiani, S. Volinia, I. Nenci, G. A. Calin, P. Querzoli, M. Negrini, and C. M. Croce, "MicroRNA gene expression deregulation in human breast cancer," *Cancer Res.*, vol. 65, pp. 7065–7070, 2005.
- [9] A. Afework, M. D. Beynon, F. Bustamante, S. Cho, A. Demarzo, R. Ferreira, R. Miller, M. Silberman, J. Saltz, A. Sussman, and H. Tsang, "Digital dynamic telepathology—The virtual microscope," in *Proc. Amer. Med. Informat. Assoc.*, 1998, pp. 912–916.
- [10] B. Molnar, L. Berczi, C. Diczfazy, A. Tagscherer, S. V. Varga, B. Szende, and Z. Tulassay, "Digital slide and virtual microscopy based on routine and telepathology evaluation of routine gastrointestinal biopsy specimens," *J. Clin. Pathol.*, vol. 56, pp. 433–438, 2003.
- [11] M. Lundin, J. Lundin, and J. Isola, "A digital atlas of breast histopathology: An application of web based virtual microscopy," *J. Clin. Pathol.*, vol. 57, pp. 1288–1291, 2004.
- [12] M. Datar, D. Padfield, and H. Cline, "Color and texture based segmentation of molecular pathology images using HSOMs," in *Proc. IEEE Int. Symp. Biomed. Imag.*, 2008, pp. 292–295.

- [13] T. Amaral, S. McKenna, K. Robertson, and A. Thompson, "Classification of breast-tissue microarray spots using colour and local invariants," in *Proc. IEEE Int. Symp. Biomed. Imag.*, 2008, pp. 999–1002.
- [14] A. Hafiane, F. Bunyak, and K. Palaniappan, "Evaluation of level set-based histology image segmentation using geometric region criteria," in *Proc. IEEE Int. Symp. Biomed. Imag.*, 2009, pp. 1–4.
- [15] X. Zhou, K. Y. Liu, N. Bradley, N. Perrimon, and S. T. Wong, "Towards automated cellular image segmentation for RNAi genome-wide screening," in *Proc. Med. Image Comput. Comput. Assist. Intervent.*, 2005, pp. 885–892.
- [16] R. Rodríguez, T. E. Alarcón, and O. Pacheco, "A new strategy to obtain robust markers for blood vessels segmentation by using the watersheds method," *Comput. Biol. Med.*, vol. 35, no. 8, pp. 665–686, 2005.
- [17] C. Wahlby, J. Lindblad, M. Vondrus, E. Bengtsson, and L. Björkstén, "Algorithms for cytoplasm segmentation of fluorescence labelled cells," *Anal. Cell. Pathol.*, vol. 24, pp. 101–111, 2002.
- [18] G. Lin, M. K. Chawla, K. Olson, J. F. Guzowski, C. A. Barnes, and B. Roysam, "Hierarchical, model-based merging of multiple fragments for improved three-dimensional segmentation of nuclei," *Cytometry*, vol. 63, pp. 20–33, 2005.
- [19] W. Yu, H. Lee, S. Hariharan, W. Y. Bu, and S. Ahmed, "Quantitative neurite outgrowth measurement based on image segmentation with topological dependence," *Cytometry*, vol. 75, pp. 289–297, 2009.
- [20] W. Yu, H. K. Lee, S. Hariharan, W. Bu, and S. Ahmed, "Evolving generalized Voronoi diagrams for accurate cellular image segmentation," *Cytometry*, vol. 77, pp. 379–386, 2010.
- [21] T. R. Jones, A. Carpenter, and P. Golland, "Voronoi-based segmentation of cell on image manifolds," *Comput. Vis. Biomed. Image Appl.*, vol. 3765, pp. 535–543, 2005.
- [22] G. Li, T. Liu, A. Tarokh, J. Nie, L. Guo, A. Mara, S. Holley, and S. T. C. Wong, "3D cell nuclei segmentation based on gradient flow tracking," *Bio. Med. Central Cell Biol.*, vol. 8, pp. 1–10, 2007.
- [23] Q. Wen, H. Chang, and B. Parvin, "A delaunay triangulation approach for segmenting clumps on nuclei," in *Proc. IEEE Int. Symp. Biomed. Imag.*, 2009, pp. 9–12.
- [24] S. Kothari, Q. Chaudry, and W. D. Wang, "Automated cell counting and cluster segmentation using convexity detection and ellipse fitting techniques," in *Proc. IEEE Int. Symp. Biomed. Imag.*, 2009, pp. 795–798.
- [25] G. Diaz, F. Gonzalez, and E. Romero, "Automatic clump splitting for cell quantification in microscopical images," *Progr. Pattern Recognit., Image Anal. Appl.*, vol. 1, pp. 763–772, 2007.
- [26] L. Yang, O. Tuzel, P. Meer, and D. J. Foran, "Automatic image analysis of histopathology specimens using concave vertex graph," in *Proc. Int. Conf. Med. Image Comput. Comput. Assist. Intervent.*, 2008, vol. 5241, pp. 833–841.
- [27] G. M. Faustino, M. Gattass, S. Rehen, and C. J. P. Lucena, "Automatic embryonic stem cells detection and counting method in fluorescence microscopy images," in *Proc. IEEE Int. Symp. Biomed. Imag.*, 2009, pp. 799–802.
- [28] C. Chen, H. Li, X. Zhou, and S. T. C. Wong, "Constraint factor graph cut-based active contour method for automated cellular image segmentation in RNAi screening," *J. Microsc.*, vol. 230, pp. 177–191, 2008.
- [29] S. Nasr-Isfahani, A. Mirasfian, and A. Masoudi-Nejad, "A new approach for touching cells segmentation," in *Proc. Int. Conf. BioMed. Eng. Inform.*, 2008, vol. 1, pp. 816–820.
- [30] M. Elter, V. Daum, and T. Wittenberg, "Maximum-intensity-linking for segmentation of fluorescence-stained cells," in *Proc. Microsc. Image Anal. Appl. Biol.*, 2006, pp. 46–50.
- [31] Y. Al-Kofahi, W. Lassoued, W. Lee, and B. Roysam, "Improved automatic detection and segmentation of cell nuclei in histopathology images," *IEEE Trans. Biomed. Eng.*, vol. 57, no. 4, pp. 841–852, Apr. 2010.
- [32] R. Malladi, J. A. Sethian, and B. C. Vemuri, "Shape modeling with front propagation: A level set approach," *IEEE Trans. Pattern Anal. Mach. Intell.*, vol. 17, no. 2, pp. 158–174, Feb. 1995.
- [33] H. K. Zhao, T. F. Chan, B. Merriman, and S. Osher, "A variational level set approach to multiphase motion," *J. Comput. Phys.*, vol. 127, pp. 179–195, 1996.
- [34] S. Osher and J. A. Sethian, "Fronts propagating with curvature-dependent speed: Algorithms based on Hamilton–Jacobi formulations," *J. Comput. Phys.*, vol. 79, pp. 12–49, 1998.
- [35] L. A. Vese and T. F. Chan, "A multiphase level set framework for image segmentation using the Mumford and shah model," *Int. J. Comput. Vis.*, vol. 50, pp. 271–293, 2002.
- [36] B. Zhang, C. Zimmer, and J. C. Olivo-Marin, "Tracking fluorescent cells with coupled geometric active contours," in *Proc. Int. Symp. Biomed. Imag.*, 2004, vol. 1, pp. 476–479.
- [37] A. Dufour, V. Shinin, S. Tajbakhsh, N. Guillen-Aghion, J. C. Olivo-Marin, and C. Zimmer, "Segmenting and tracking fluorescent cells in dynamic 3D microscopy with coupled active surfaces," *IEEE Trans. Image Process.*, vol. 14, no. 9, pp. 1396–1410, Sep. 2005.
- [38] P. Yan, X. Zhou, M. Shah, and S. T. C. Wong, "Automatic segmentation of high-throughput RNAi fluorescent cellular images," *IEEE Trans. Inf. Technol. Biomed.*, vol. 12, no. 1, pp. 109–117, Jan. 2008.
- [39] X. Qi, F. King, D. J. Foran, and L. Yang, "GPU enabled parallel touching cell segmentation using mean shift based seed detection and repulsive level set," in *Proc. High Perform. Comput. (HP) Workshop Assoc. Proc. Int. Conf. Med. Image Comput. Comput. Assist. Intervent. (MICCAI)*, 2010.
- [40] W. Chen, M. Reiss, and D. J. Foran, "A prototype for unsupervised analysis of tissue microarrays for cancer research and diagnostics," *IEEE Trans. Inf. Technol. Biomed.*, vol. 8, no. 2, pp. 89–96, Jun. 2004.
- [41] D. J. Foran, L. Yang, O. Tuzel, W. Chen, J. Hu, T. Kurc, R. Ferreira, and J. Saltz, "A caGrid-enabled, learning based image segmentation method for histopathology specimens," in *Proc. Int. Symp. Biomed. Imag.*, 2009, pp. 1306–1309.
- [42] B. Parvin, Q. Yang, J. Han, H. Chang, B. Rydberg, and M. H. Barcellos-Hoff, "Iterative voting for inference of structural saliency and characterization of subcellular events," *IEEE Trans. Image Process.*, vol. 16, no. 3, pp. 615–623, Mar. 2007.
- [43] T. F. Chan and L. A. Vese, "Active contours without edges," *IEEE Trans. Image Process.*, vol. 10, no. 2, pp. 266–277, Feb. 2001.
- [44] R. Baeza-Yates and B. Ribeiro-Neto, *Modern Information Retrieval*, 1st ed. Reading, MA: Addison-Wesley, 2005.
- [45] L. Grady and E. L. Schwartz, "Isoperimetric graph partitioning for image segmentation," *IEEE Trans. Pattern Anal. Mach. Intell.*, vol. 28, no. 1, pp. 469–475, Mar. 2006.

Authors' photographs and biographies not available at the time of publication.